ARTICLE

Pressure-Stimulus-Responsive Behaviors of Core–Shell InP/ZnSe Nanocrystals: Remarkable Piezochromic Luminescence and Structure Assembly

Received 00th January 20xx,
Accepted 00th January 20xx

DOI: 10.1039/x0xx00000x

Hao Liu,[a, b] Yixuan Wang,[a] Xinyi Yang,*[a] Xiaohui Zhao,[a] Kai Wang,[a] Min Wu,[a] Xiaobing Zuo,[c] WengYang,[d] Yongming Sui,*[a] and Bo Zou*[a]

Piezochromic luminescence materials that their optical properties can be adjusted (especially, the most sensitive color ranges from red to green of the human eye), provide powerful means for information acquisition in various applications. Inorganic quantum dots, typically based on heavy metals such as cadmium and lead, have congenital advantages as luminescence materials, including strong inoxidizability and excellent photoelectric properties. However, small band-gap shifts under pressure have hindered development of inorganic-based piezochromic materials. Here, we combine *in situ* high-pressure photoluminescence (PL) and absorption measurements with synchrotron X-ray scattering spectra to elucidate the remarkable modulation of optical properties and morphologies by pressure, particularly that of the piezochromic luminescence, in all-inorganic core–shell InP/ZnSe nanocrystals (NCs). We observed a stepwise PL color changed from red to green and an ultrabroad bandgap tunability of 0.46 eV was observed from 1.99 to 2.45 eV in the pressure range of 14.2 GPa for InP/ZnSe NCs. Moreover, two-dimensional (2D) InP/ZnSe nanosheets were synthesized by stress-driven attachment of nanoparticles. These results demonstrate the ability of the pressure-stimulus response to trigger remarkable piezochromic luminescence and 2D nanosheet assembly in InP/ZnSe NCs, which paves the way for new applications of all-inorganic InP-based semiconductor NCs.

Introduction

Inorganic semiconductor quantum dots (QDs) have emerged as an interesting class of luminescent materials because of their unique optical properties, such as high photoluminescence (PL) quantum yields, good photochemical stability and precisely tunable emission.[1-2] Such properties also make them potentially useful for light-emitting diodes, infrared photodetection, solar energy conversion, etc.[3-6] Following the restrictions on Cd and Pb, III–V semiconductor InP QDs have become viable alternatives, which exhibit tunable emission covered the visible-to-near-infrared region.[2, 7-8] By means of constructing core-shell heterostructures with ZnSe shell, the PL performance of InP QDs can be boosted due to the passivation of defects and suppression of oxidation from the core surface.[9-10] Moreover, the thick shell also effectively suppresses blinking and Auger recombination within InP QDs.[11-12] In the core–shell heterostructures, the epitaxially grown shell typically produces tensile or compressive strains on the core, attributable to the lattice mismatch.[13-17] The tensile and/or compressive strains alter the lattice constant (interatomic distance) and modify the electronic energy gap, such that their electronic and optical properties can be regulated significantly.[18-21]

Similar to the compressive strain, the application of an external pressure can precisely alter the intrinsic interatomic distances and therefore modify the energy positions of the valence and conduction bands.[22-24] These changes have significant influences on their absorption and emission properties.[25-29] Such pressure-stimulus optical responsive characteristic provides powerful means for information acquisition in various applications, from pressure sensing, anticounterfeiting, to optoelectronic memory.[29-30] Up to now, piezochromic luminescent materials have been mainly focused on organic polymers and compounds containing organic molecules, whereas they suffer from instability under ambient conditions.[30-32] All-inorganic semiconductor nanocrystals (NCs) have the strong ability to resist photooxidation,[10, 33] however, there is a formidable challenge to develop all-inorganic semiconductor NCs that could exhibit dynamic colour tunability, especially, the most sensitive color ranges from red to green of the human eye, in response to variations in pressure.[34] In III–V semiconductors, the *s*-orbital and *p*-orbital states occupy the conduction band minimum (CBM) and valence band maximum (VBM), respectively. The *s* orbitals are more affected by the interatomic distance variation than the *p* orbital.[19] The application of external pressure causes a decrease in the intrinsic interatomic distances, resulting in a rapid increase of the conduction band energy.[19] Our previous reports have confirmed that InP/ZnS NCs have remarkable piezochromic behavior, where color change from orange to green.[26]

[a] State Key Laboratory of Superhard Materials, College of Physics, Jilin University, Changchun, 130012, China. E-mail: yangxinyi@jlu.edu.cn, suiym@jlu.edu.cn, zoubo@jlu.edu.cn
[b] School of Physics and Electronic Engineering, Xinxiang University, Xinxiang 453003, China
[c] X-ray Science Division, Advanced Photon Source, Argonne National Laboratory, Lemont, IL 60439, United States
[d] Center for High-Pressure Science and Technology Advanced Research, Beijing 100094, China

† Electronic Supplementary Information (ESI) available: General Information, Figures and Tables. CCDC 2121372. See DOI: 10.1039/x0xx00000x

Compared with the 7.7 % lattice mismatch rate between ZnS and InP, the lattice mismatch rate between ZnSe and InP is only 3.2 %.[1] This makes InP/ZnSe have a narrow emission spectrum compared to InP/ZnS and ensures the luminescence purity of InP/ZnSe NCs, thus providing more pronounced color changes for piezochromic behavior studies. The low lattice mismatch also makes it easier for ZnSe to epitaxially grow on the InP core and precisely adjusts the size of the core-shell structured NPs. Moreover, ZnSe has a smaller bulk modulus (62.4 GPa) compared to ZnS (77.1 GPa).[19] This means that the lattice of ZnSe is readily compressed and its electronic energy bands shift to a large degree under compression. We therefore speculate that broadly tunable piezochromic luminescence may be induced in core–shell InP/ZnSe NCs by precisely manipulating the interatomic distance.

In this study, we loaded InP/ZnSe NCs into a diamond anvil cell (DAC) and systematically studied their optical properties under pressure using *in situ* PL and absorption spectra. Under a pressure of 0 to 5.6 GPa, the PL color of the InP/ZnSe NCs gradually changed from red (619 nm) to green (546 nm). To the best of our knowledge, this is the largest piezochromic PL tuning range in the visible light range for traditional inorganic semiconductor nanomaterials.[26, 35-36] Simultaneously, an ultrabroad bandgap tunability range was observed from 1.99 eV (0 GPa) to 2.45 eV (~14.2 GPa). In addition, *in situ* small-angle synchrotron X-ray scattering (SAXS) measurements and transmission electron microscopy (TEM) images demonstrated that core–shell InP/ZnSe NCs were sintered under high pressure, resulting in the formation of two-dimensional (2D) nanostructures. Our findings enrich the understanding of the relationship between the optical properties and morphology of the InP/ZnSe NCs and pave the way for their future applications in piezochromic luminescence.

Results and discussion

Preparation and Characterization of InP/ZnSe NCs

We synthesized core–shell InP/ZnSe NCs through a modified procedure (see Supporting Information).[37] The synthesis involves two main steps: (I) the preparation of InP core and (II) the epitaxial growth of the ZnSe shell on InP core. Imaging of the NCs using TEM shows that, following ZnSe shell growth, the average diameter of the particles increases from 2.5 (SE 0.1) nm for the InP core (Fig S2) to 6.2 (SE 0.1) nm (Fig 1a),

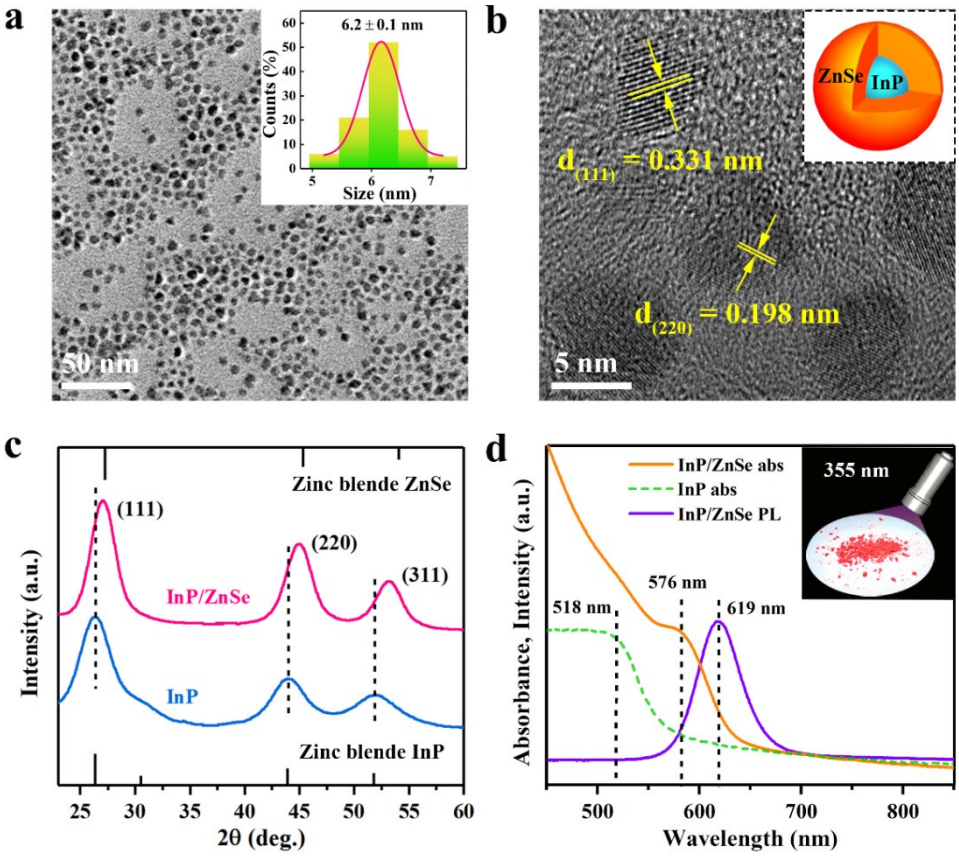

Fig. 1 (a) Representative TEM image of the InP/ZnSe NCs. Inset: corresponding size distribution histogram. For size distribution, at least 300 NPs were analyzed, from 3 areas on the sample TEM grid. The average size of the InP/ZnSe NCs was 6.2 nm with a standard error (SE) of 0.1 nm. (b) High-resolution (HR) TEM image of the InP/ZnSe NCs. Inset: schematic of the core–shell InP/ZnSe NC. (c) Angle-dispersive X-ray diffraction (ADXRD) patterns of the core InP and core–shell InP/ZnSe NCs. (d) Ambient ultraviolet–visible (UV–vis) absorbance spectra of InP NCs (green dotted line) and InP/ZnSe NCs (orange solid line) together with the PL spectrum of InP/ZnSe NCs (violet solid line). Inset: corresponding photograph of InP/ZnSe NCs under UV irradiation (λ_{ex} = 355 nm).

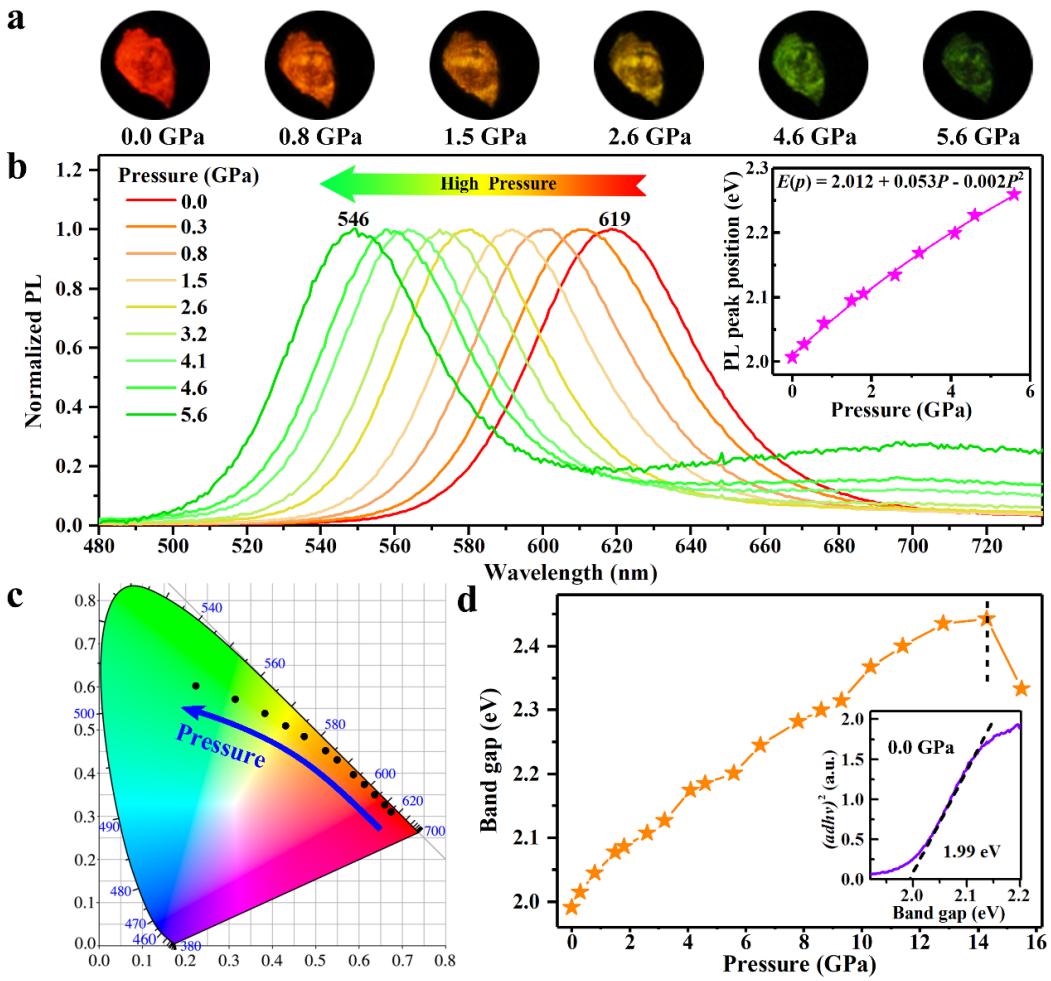

Fig. 2 (a) PL microscopic images of the InP/ZnSe NCs under high pressures. A UV light was used for the excitation (λ_{ex} = 355 nm). (b) PL peak position changes from 619 to 546 nm with the increase in the pressure from 0 to 5.6 GPa. Inset: PL peak position as a function of pressure. (c) Pressure-dependent chromaticity coordinates of the emissions. (d) Shift of the bandgap energy with pressure. Inset shows the Tauc plot of the InP/ZnSe NCs under ambient conditions.

corresponding to a shell thickness of ~1.9 nm (~6 monolayers). According to the HRTEM image (Fig 1b), the synthesized InP/ZnSe NCs reveal a high crystallinity with continuous lattice fringes throughout the whole particle. The XRD pattern confirms that the InP phase is consistent with that of bulk zinc blende (ZB) InP (Fig 1c, blue). The core–shell samples exhibit diffraction peak shifts toward higher 2θ angles compared to that of ZB-type InP. The lattice parameter of ZnSe shell (5.67 Å) is smaller than that of the InP core (5.87 Å),[1] which results in a contraction of the crystal lattice, attributable to the compressive strain induced by the heteroepitaxial ZnSe shell. The optical properties of the InP and InP/ZnSe NCs were investigated via absorption and PL spectra, as shown in Fig 1d. Compared to the InP core (518 nm), the absorption of InP/ZnSe NCs is red-shifted to 576 nm (by 0.2 eV). The InP NCs show weak and broad emission in the 500–900 nm region including both band edge and trap-mediated emissions (Fig S3). By contrast, the InP/ZnSe NCs exhibit obvious band edge emission peak at about 619 nm with full width at half-maximum of 51 nm, which results from the passivation of the surface trap states in InP by the epitaxial growth of the ZnSe shell. The InP/ZnSe NCs exhibit bright red PL under 355 nm UV light (inset of Fig 1d) and dark brown under daylight (Fig S4).

In situ High-Pressure PL Propertie of InP/ZnSe NCs

We employed the Mao-Bell-type symmetric DAC as a high-pressure generator (see Supporting Information).[38] The InP/ZnSe NCs were loaded into the DAC chamber along with a ruby ball and silicon oil (150 cst, Aldrich). The actual pressure was measured using the standard ruby fluorescence technique.[39] The silicon oil was utilized as the pressure-transmitting medium (PTM) to provide a hydrostatic environment.[40] When the pressure was applied to the InP/ZnSe NCs, the PL color of the sample gradually changed from bright red to dark green. A series of PL micrographs of the InP/ZnSe NCs were obtained from the DAC interior under the same laser excitation (Fig 2a). The evolution of the PL spectra of the InP/ZnSe NCs with applied pressure are presented in Fig 2b. The PL peak position of the InP/ZnSe NCs exhibits a continuous blue shift from 619 nm (0 GPa) to 546 nm (5.6 GPa). When the pressure was released from 5.6 GPa, the PL intensity and peak position reversibly returned (Fig S5). Upon further compression, the PL peak position showed a continued blue shift until the PL

completely disappeared at 8.7 GPa (Fig S6), which is consistent with the decreasing PLQYs (Table S1). The pressure-induced PL peak energies of the InP/ZnSe NCs within 5.6 GPa are shown in the inset of Fig 2b. The following quadratic equation is used to fit the experimental data

$$E(P) = E_0 + \alpha P + \beta P^2, \quad (1)$$

where $E(P)$ is the PL peak energy and E_0 = 2.012 eV is the PL peak energy at ambient pressure, which can be obtained experimentally. The fitting parameters (pressure coefficients) α and β are 53 meV/GPa and −2 meV/GPa^2, respectively, whereas, experimental values of 75−84 meV/GPa and −1.2 to −1.8 meV/GPa^2 have been reported for α and β of the bulk ZB-type InP.[41] The decrease of α was attributed to the highly confined energy levels in the InP/ZnSe NCs.[42] Further, we recorded the pressure-dependent chromaticity coordinates of the emission from the InP/ZnSe NCs (Fig 2c). The ability to alter the emission chromaticity by high-pressure technologies indicates that the core–shell InP/ZnSe NCs have a high potential for use as piezochromic materials.

In situ High-Pressure Absorption Propertie of InP/ZnSe NCs

The pressure-dependent absorption spectra of the InP/ZnSe NCs exhibit a considerable blue-shift up to the maximum pressure of ~14.2 GPa (Fig S7). The initial blue-shift of the absorption edge could be attributed to the enhancement of quantum confinement effect due to the pressure-induced contraction of the crystal lattice.[43] When the pressure was completely released from ~14.2 GPa, the absorption spectrum indicated the absorption edge returned to its initial state (Fig S8). When a considerably higher pressure (above 14.2 GPa) was applied, an abrupt red shift of the absorption edge and a broad absorption tail at higher energies were observed (Fig S7 and S9). The red shift of the absorption edge may be explained by the phase transition and/or morphological change of the InP/ZnSe NCs under high pressure.[44] After a compression cycle of 0–21.0 GPa, the absorption edge exhibits a red-shift in comparison with the initial edge (Fig S10). Based on the *in situ* high pressure absorption spectra, the bandgaps of InP/ZnSe NCs were estimated at different pressures (Fig 2d).[45] As pressure increased, the bandgap of InP/ZnSe NCs gradually blue shifted below 14.2 GPa and an ultrabroad bandgap tunability range was generated from 1.99 to 2.45 eV. Compared with that of InP NCs changed from 2.24 (1 atm) to 2.25 eV (9.0 GPa) (Fig S11 and S12), InP/ZnSe NCs show a greater bandgap tunability range. We believe that the coating of the soft shell ZnSe makes the better elasticity of the core InP, thus allowing the regulation of a higher level in bandgap engineering. The widely and precise bandgap tunability of InP/ZnSe NCs under pressure would provide an effective access to the fabrication of InP-based sensors and switch devices.

In situ High-Pressure ADXRD Measurement

To clarify the relation between the crystal structure and optical properties of the InP/ZnSe NCs, *in situ* high-pressure ADXRD measurements were carried out. Fig 3a shows typical ADXRD patterns of the InP/ZnSe NCs during a compression cycle of 0–21.5 GPa. When the pressure was increased from 0 to 14.2 GPa, all diffraction peaks shifted to high 2θ angles and the lattice parameter decreased (Fig 3b), indicating the

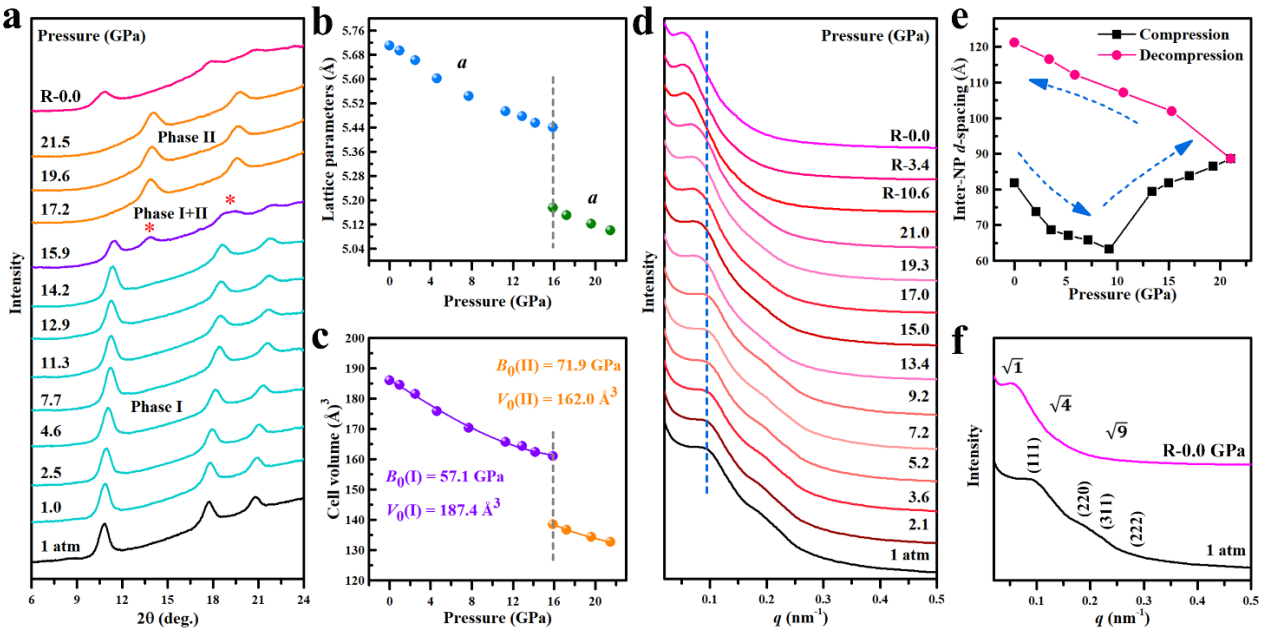

Fig. 3 (a) Representative in situ high-pressure ADXRD patterns of the InP/ZnSe NCs at various pressures. (b) The lattice parameter changes with the pressure. (c) Changes in the unit cell volume with the pressure in InP/ZnSe NCs. (d) Representative in situ high-pressure SAXS patterns of the InP/ZnSe NCs at various pressures. (e) Corresponding inter-NC distance during compression (black, peak pressure of 29.9 GPa) and decompression (pink). (f) SAXS patterns of the initial (black line) and recovered (magenta line) samples.

pressure-induced reductions of the interatomic distances. In III-V and II-VI semiconductors, this change can largely affect the overlap of wave functions, triggering the shifts of the conduction band and valence band to higher energies.[19, 23] First-principles calculations demonstrate that the CBM of bulk ZB-InP is more affected by the variation of the interatomic distance than the VBM, where the CBM has a large change, and the VBM moves slightly under compression (Fig S13). Based on the above analysis, schematic illustration of electronic energy levels for InP/ZnSe core/shell NCs are shown in Fig S14. With increasing pressure, the bandgap broadens due to a significant increase in the energy levels of CBM. Therefore, the optical absorption and PL spectra gradually shifted towards higher energies under external pressure. With a further increase in pressure, two new diffraction peaks appeared at 15.9 GPa, indicating the presence of a pressure-induced phase transition. The new phase was indexed to the rock salt (RS) phase based on Rietveld refinement results (Fig S15) and remained stable up to the highest pressure of 21.5 GPa studied in this work. The indirect bandgap of the RS phase can explain the vanishing PL and red-shifting of the absorption edge in InP/ZnSe NCs at higher pressure.[46] Subsequently, the release of the pressure caused a reversible phase transformation from the RS to ZB structure. Compared to the initial sample, the diffraction peaks of the sample after the pressure treatment became weak and widened owing to the pressure-induced distortion or amorphization of the partial lattice.[47] As shown in Fig 3c, the bulk modulus B_0 of the InP/ZnSe NCs was estimated to be 57.1 GPa before phase transition by fitting the cell volume data with the third-order Birch–Murnaghan equation of state:[48]

$$\boldsymbol{P(V)} = \frac{3}{2}\boldsymbol{B_0}\left[\left(\frac{V_0}{V}\right)^{\frac{7}{3}} - \left(\frac{V_0}{V}\right)^{\frac{5}{3}}\right]\left\{1 + \frac{3}{4}\left(B_0^{'} - 4\right)\left[\left(\frac{V_0}{V}\right)^{\frac{7}{3}} - 1\right]\right\}. \quad (2)$$

Upon compression, B_0 of the high-pressure phase in InP/ZnSe NCs is 71.9 GPa, implying a still relatively large compressibility after phase transition, which may be beneficial to bandgap engineering.[49]

***In situ* High-Pressure SAXS Measurement**

In addition to the crystal structure, the morphology of the crystal is also an important factor affecting its optical properties.[50-52] Therefore, we acquired a series of *in situ* high-pressure SAXS patterns to investigate the mesostructures of the InP/ZnSe NCs. Figs 3d and 3e show typical SAXS patterns of the InP/ZnSe NCs and calculated *d*-spacings of the first Bragg reflection of the SAXS at various pressures, respectively. When the pressure was increased from 0 to 9.0 GPa, all SAXS peaks shifted to higher *q* positions. Concomitantly, the *d*-spacing was reduced from 83 to 63 Å (Fig 3e). The continuous increase in the pressure led to reversed shifts in the *d*-spacing, which indicated that the InP/ZnSe NCs underwent a pressure-driven detachment and rearrangement of surface ligands.[50] Notably, the threshold pressure of ~9.0 GPa was close to the PL quenching pressure of 8.7 GPa. This suggested that the detachment and rearrangement of surface ligands facilitated the PL weakening. During the assembly of NPs, pressure-induced lattice distortion and bending of chemical bonds can increase defect states, thus the PL became weaken and finally disappeared. When the pressure was reduced to ambient pressure, the *d*-spacing of the SAXS peak did not return to 83 Å; instead, it continuously increased to 120 Å. Concomitantly, several adjacent SAXS peaks merged and the number of peaks was reduced to 3 (Fig 3f). The three remaining peaks exhibited a linear correlation of q/q_0 =1/2/3, indicating the formation of a lamellar mesostructure.[53-54]

TEM and HRTEM Characterizations of InP/ZnSe Nanosheets

To verify that the InP/ZnSe NCs were sintered under high pressure and formed a lamellar mesostructure, we also performed TEM and HRTEM characterizations. Upon pressure release, the recovered samples were carefully removed from the DAC metal gasket, dispersed by the proper amount of toluene, and then transferred to a copper grid for characterization. After decompression from 21.1 GPa, the TEM images (Fig 4a) evidenced the formation and preservation of pressure-driven lamellar InP/ZnSe nanosheets. The nanosheets had an irregular geometry. The average size of the InP/ZnSe nanosheets was 139.9 nm (SE 9.2 nm). The HRTEM image (Fig 4b) showed a smooth nanosheet with the fusion of multiple NCs. The typical lattice fringe spacing was ~0.33 nm, which corresponded to the lattice spacing of the (111) planes of the initial InP/ZnSe NCs. In addition, some irregular stripes were observed owing to particle fusion driven by deviatoric stress.[55] The thickness of the InP/ZnSe nanosheets was approximately 27.5 nm (see Supporting Information), equivalent to the thickness of several initial NCs.

Fig 4c shows a schematic of a possible model for the InP/ZnSe nanosheet based on the HRTEM image. Driven by the external pressure, the InP/ZnSe NCs are assembled to form a gumdrop-cake-like nanosheet structure. The formation of the InP/ZnSe nanosheet is illustrated in Fig 4d. Under ambient conditions, the InP/ZnSe NCs maintained an ordered monodispersity owing to the equilibrium among the hydrophobic attractions, van der Waals forces, and charge–charge interactions. Upon compression with low pressure (<9 GPa), the pressure was insufficient to break the force balance among adjacent NCs, where the InP/ZnSe NCs remained monodispersed (Fig S16a).[22-23] Nonetheless, the pressure-induced lattice distortion and bending of chemical bonds disrupted the crystal field. And the overlap of the wave functions between atoms disordered.[31] Thus, the PL weakened by the application of pressure. This phenomenon is repairable, according to the recovery of the PL and absorption after the pressure release (Fig 4e, left). Further compression breaks the force balance among adjacent NCs and drives the NCs to contact. However, the TEM image of the sample acquired after releasing the pressure from 14.2 GPa shows that the NCs maintain the monodispersity owing to the instability of this contact (Fig S16b). The PL peak position and absorption edge returned to the initial positions (Fig 4e, middle). The PL intensity was reduced to approximately 50% of the initial value because of the increase in number of surface

defect states by the separation of ligands from the NCs surfaces after the

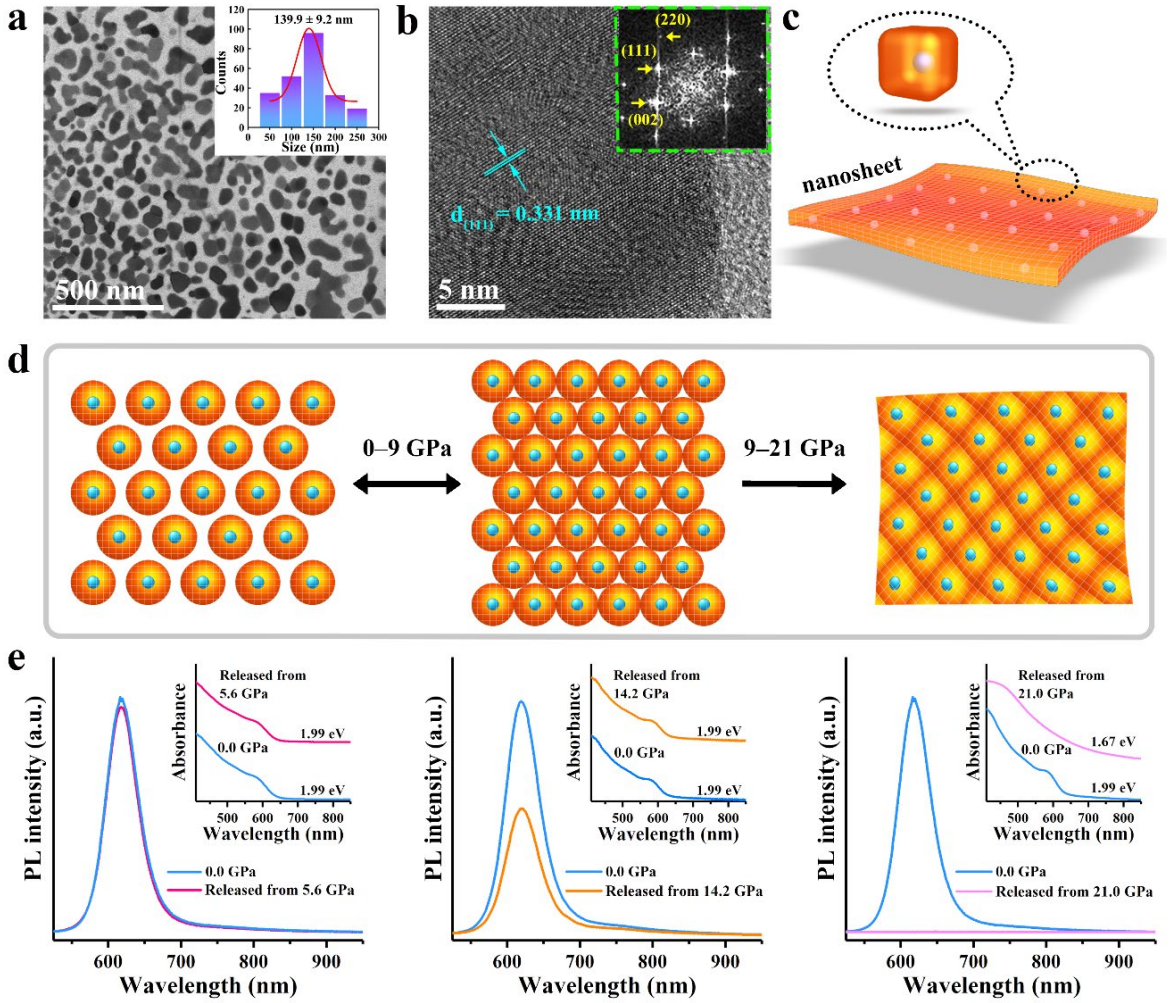

Fig. 4 (a) Representative TEM image of the 2D InP/ZnSe nanosheets, acquired after releasing the pressure from 21.1 GPa. Inset: corresponding size distribution histogram. For size distribution, at least 200 nanosheets were analyzed, from 3 areas on the sample TEM grid. The average size of the InP/ZnSe nanosheets was 139.9 nm with a SE of 9.2 nm. (b) HRTEM image of the InP/ZnSe nanosheet. Inset: corresponding fast Fourier transform pattern. (c) Schematic of the InP/ZnSe nanosheet. (d) Schematic of the formation of the pressure-driven 2D lamellar mesostructure. (e) Comparisons of the PL and absorption spectra in the InP/ZnSe NCs before and after the compression.

pressure treatment.[56] With the increase pressure to 21.1 GPa, the InP/ZnSe NCs changed to the RS phase. Upon the decompression from 21.1 GPa, the InP/ZnSe NCs recovered to the initial ZB phase. The TEM image shows the formation of nanosheets. Simultaneously, the PL of the InP/ZnSe NCs completely disappeared (Fig 4e, right), which can be attributed to the increase in number of defect states due to pressure-induced lattice distortion and bending of chemical bonds.[56] This pressure-induced fluorescence quenching and its irreversibility also occur in a better hydrostatic pressure environment using nitrogen as the PTM. The absorption edge exhibited a red-shift in comparison with the initial edge, which originated from the reduced quantum confinement owing to the formation of the nanosheets.[44]

Conclusions

In summary, the all-inorganic core–shell InP/ZnSe NCs exhibited remarkable optical and morphological changes in response to the external stimulus of high pressure. Below 5.6 GPa, their PL spectrum blue shifted greatly with increasing applied pressure and the PL color changed from red (619 nm) to green (546 nm). This PL blue-shift tunability is fully reversible and immediately responds to pressure changes. Simultaneously, a widely bandgap tunability range is generated, starting from 1.99 eV at 0 GPa to 2.45 eV at about 14.2 GPa. In addition, the *in situ* SAXS patterns and TEM images confirmed that core–shell InP/ZnSe NCs were sintered under high pressure, transforming into lamellar mesostructures. Our work has enriches the understanding of the pressure-dependent optical and structural assembly in all-inorganic core–shell NCs, which might open up new opportunities to fabricate piezochromic materials based on all-inorganic semiconductors.

Author Contributions

H.L., Y.W., X.Y., X.Z., Y.S. and B.Z. designed and performed experiments and analyzed data. M.W., K.W., X.Z. and W.Y. assisted in performing experiments. H.L., X.Y., Y.S. and B.Z. wrote the manuscript.

Conflicts of interest

There are no conflicts to declare.

Acknowledgements

This study was supported by the National Natural Science Foundation of China (Nos. 11874027, 21725304 and 11774124), Chang Jiang Scholars Program of China (No. T2016051), and China Postdoctoral Science Foundation (Nos. 2019T120233 and 2017M621198). This study was performed mainly at BL15U1 at the Shanghai Synchrotron Radiation Facility. Parts of this study were performed at beamline 12-ID-B at the Advanced Photon Source, a US Department of Energy (DOE) Office of Science User Facility operated for the DOE Office of Science by Argonne National Laboratory under Contract DE-AC0206CH11357.

References

(1) A. Brodu, M. V. Ballottin, J. Buhot, E. J. van Harten, D. Dupont, A. La Porta, P. T. Prins, M. D. Tessier, M. A. M. Versteegh, V. Zwiller, S. Bals, Z. Hens, F. T. Rabouw, P. C. M. Christianen, C. de Mello Donega, D. Vanmaekelbergh, *ACS Photonics* **2018**, *5*, 3353−3362.
(2) P. Reiss, M. Carrière, C. Lincheneau, L. Vaure, S. Tamang, *Chem. Rev.* **2016**, *116*, 10731−10819.
(3) Y. H. Won, O. Cho, T. Kim, D. Y. Chung, T. Kim, H. Chung, H. Jang, J. Lee, D. Kim, E. Jang, *Nature* **2019**, *575*, 634−638.
(4) Xingliang, Z. Zhang, Y. Jin, Y. Niu, H. Cao, X. Liang, L. Chen, J. Wang, X. Peng, *Nature* **2014**, *515*, 96−99.
(5) G. Konstantatos, I. Howard, A. Fischer, S. Hoogland, J. Clifford, E. Klem, L. Levina, E. Sargent, *Nature* **2006**, *442*, 180−183.
(6) N. Yaacobi-Gross, M. Soreni-Harari, M. Zimin, S. Kababya, A. Schmidt, N. Tessler, *Nat. Mater.* **2011**, *10*, 974−979.
(7) Z. Xu, Y. Li, J. Li, C. Pu, J. Zhou, L. Lv, X. Peng, *Chem. Mater.* **2019**, *31*, 5331−5341.
(8) P. Ramasamy, N. Kim, Y.-S. Kang, O. Ramirez, J. S. Lee, *Chem. Mater.* **2017**, *29*, 6893−6899.
(9) J. M. Pietryga, Y. S. Park, J. Lim, A. F. Fidler, W. K. Bae, S. Brovelli, V. I. Klimov, *Chem. Rev.* **2016**, *116*, 10513−10622.
(10) M. D. Tessier, E. A. Baquero, D. Dupont, V. Grigel, E. Bladt, S. Bals, Y. Coppel, Z. Hens, C. Nayral, F. Delpech, *Chem. Mater.* **2018**, *30*, 6877−6883.
(11) Y. Li, X. Hou, X. Dai, Z. Yao, L. Lv, Y. Jin, X. Peng, *J. Am. Chem. Soc.* **2019**, *141*, 6448−6452.
(12) K. R. Reid, J. R. McBride, N. J. Freymeyer, L. B. Thal, S. J. Rosenthal, *Nano Lett.* **2018**, *18*, 709−716.
(13) L. Jing, S. V. Kershaw, T. Kipp, S. Kalytchuk, K. Ding, J. Zeng, M. Jiao, X. Sun, A. Mews, A. L. Rogach, M. Gao, *J. Am. Chem. Soc.* **2015**, *137*, 2073−2084.
(14) F. Fan, O. Voznyy, R. P. Sabatini, K. T. Bicanic, M. M. Adachi, J. R. McBride, K. R. Reid, Y. S. Park, X. Li, A. Jain, R. Quintero-Bermudez, M. Saravanapavanantham, M. Liu, M. Korkusinski, P. Hawrylak, V. I. Klimov, S. J. Rosenthal, S. Hoogland, E. H. Sargent, *Nature* **2017**, *544*, 75−79.
(15) M. Rafipoor, D. Dupont, H. Tornatzky, M. D. Tessier, J. Maultzsch, Z. Hens, H. Lange, *Chem. Mater.* **2018**, *30*, 4393−4400.
(16) A. Hazarika, I. Fedin, L. Hong, J. Guo, V. Srivastava, W. Cho, I. Coropceanu, J. Portner, B. T. Diroll, J. P. Philbin, E. Rabani, R. Klie, D. V. Talapin, *J. Am. Chem. Soc.* **2019**, *141*, 13487−13496.
(17) D. D. Sarma, A. Nag, P. K. Santra, A. Kumar, S. Sapra, P. Mahadevan, *J. Phys. Chem. Lett.* **2010**, *1*, 2149−2153.
(18) A. M. Smith, A. M. Mohs, S. Nie, *Nature Nanotechnol.* **2009**, *4*, 56−63.
(19) S. H. Wei, A. Zunger, *Phys. Rev. B* **1999**, *60*, 5404−5411.
(20) A. Hazarika, A. Pandey, D. D. Sarma, *J. Phys. Chem. Lett.* **2014**, *5*, 2208−2213.
(21) Y. S. Park, J. Lim, V. I. Klimov, *Nat. Mater.* **2019**, *18*, 249−255.
(22) F. Bai, K. Bian, X. Huang, Z. Wang, H. Fan, *Chem. Rev.* **2019**, *119*, 7673−7717.
(23) Y. H. Li, X. G. Gong, S.-H. Wei, *Phys. Rev. B* **2006**, *73*, 245206.
(24) X. Lü, C. Stoumpos, Q. Hu, X. Ma, D. Zhang, S. Guo, J. Hoffman, K. Bu, X. Guo, Y. Wang, C. Ji, H. Chen, H. Xu, Q. Jia, W. Yang, M. G. Kanatzidis, H.-K. Mao, *Nati. Sci. Rev.* **2021**, *8*, nwaa288.
(25) S. Guo, K. Bu, J. Li, Q. Hu, H. Luo, Y. He, Y. Wu, D. Zhang, Y. Zhao, W. Yang, M. G. Kanatzidis, X. Lü, *J. Am. Chem. Soc.* **2021**, *143*, 2545−2551.
(26) H. Liu, X. Yang, K. Wang, Y. Wang, M. Wu, X. Zuo, W. Yang, B. Zou, *ACS Appl. Nano Mater.* **2020**, *3*, 2438−2446.
(27) B. Li, K. Bian, X. Zhou, P. Lu, S. Liu, I. Brener, M. Sinclair, T. Luk, H. Schunk, L. Alarid, P. G. Clem, Z. Wang, H. Fan, *Sci. Adv.* **2017**, *3*, e1602916.
(28) L. Wang, P. Yao, F. Wang, S. Li, Y. Chen, T. Xia, E. Guo, K. Wang, B. Zou, H. Guo, *Adv. Sci.* **2020**, *7*, 1902900.
(29) Q. Zhang, J. Su, D. Feng, Z. Wei, X. Zou, H. C. Zhou, *J. Am. Chem. Soc.* **2015**, *137*, 10064−10067.
(30) C. X. Chen, Z. W. Wei, Y. N. Fan, P. Y. Su, Y. Y. Ai, Q. F. Qiu, K. Wu, S. Y. Yin, M. Pan, C. Y. Su, *Chem* **2018**, *4*, 2658−2669.
(31) S. Liu, S. Sun, C. K. Gan, A. G. del Águila, Y. Fang, J. Xing, T. T. H. Do, T. J. White, H. Li, W. Huang, Q. Xiong, *Sci. Adv.* **2019**, *5*, eaav9445.
(32) L. Wang, K. Wang, B. Zou, K. Ye, H. Zhang, Y. Wang, *Adv. Mater.* **2015**, *27*, 2918−2922.
(33) P. Reiss, M. Protière, L. Li, *Small* **2009**, *5*, 154−168.
(34) C. L. Choi, K. J. Koski, S. Sivasankar, A. P. Alivisatos, *Nano Lett.* **2009**, *9*, 3544−3549.
(35) G. Xiao, Y. Wang, D. Han, K. Li, X. Feng, P. Lv, K. Wang, L. Liu, S. A. T. Redfern, B. Zou, *J. Am. Chem. Soc.* **2018**, *140*, 13970−13975.
(36) H. Liu, X. Zhao, X. Yang, Y. Wang, M. Wu, J. Jiang, G. Wu, K. Yuan, L. Sui, B. Zou, *Nanoscale Horiz.* **2020**, *5*, 1233−1239.
(37) M. D. Tessier, D. Dupont, K. De Nolf, J. De Roo, Z. Hens, *Chem. Mater.* **2015**, *27*, 4893−4898.
(38) H. Mao, P. Bell, K. Dunn, R. Chrenko, R. DeVries, *Rev. Sci. Instrum.* **1979**, *50*, 1002−1009.
(39) H. K. Mao, J. Xu, P. M. Bell, *J. Geophys. Res.* **1986**, *91*, 4673−4676.
(40) S. Klotz, J. C. Chervin, P. Munsch, G. Marchand, *J. Phys. D: Appl. Phys.* **2009**, *42*, 075413.
(41) N. Chauvin, A. Mavel, G. Patriarche, B. Masenelli, M. Gendry, D. Machon, *Nano Lett.* **2016**, *16*, 2926−2930.
(42) V. A. Wilkinson, A. D. Prins, D. J. Dunstan, L. K. Howard, M. T. Emeny, *J. Elec. Mater.* **1991**, *20*, 509−516.
(43) S. Yang, D. Prendergast, J. B. Neaton, *Nano Lett.* **2010**, *10*, 3156−3162.

(44) W. E. Buhro, V. L. Colvin, *Nat. Mater.* **2003**, *2*, 138−139.
(45) J. Tauc, R. Grigorovici, A. Vancu, *phys. stat. sol.* **1966**, *15*, 627−637.
(46) J. G. Díaz, G. W. Bryant, W. Jaskólski, M. Zieliński, *Phys. Rev. B* **2007**, *75*, 245433.
(47) M. Xu, W. Zhang, R. Mazzarello, M. Wuttig, *Adv. Sci.* **2015**, *2*, 1500117.
(48) F. Birch, *Phys. Rev.* **1947**, *71*, 809−824.
(49) L. Zhang, C. Liu, L. Wang, C. Liu, K. Wang, B. Zou, *Angew. Chem.* **2018**, *130*, 11383−11387; *Angew. Chem. Int. Ed.* **2018**, *57*, 11213−11217.
(50) Y. Nagaoka, K. Hills-Kimball, R. Tan, R. Li, Z. Wang, O. Chen, *Adv. Mater.* **2017**, *29*, 1606666.
(51) B. Li, X. Wen, R. Li, Z. Wang, P. G. Clem, H. Fan, *Nat. Commun.* **2014**, *5*, 4179.
(52) L. Meng, J. M. D. Lane, L. Baca, J. Tafoya, T. Ao, B. Stoltzfus, M. Knudson, D. Morgan, K. Austin, C. Park, P. Chow, Y. Xiao, R. Li, Y. Qin, H. Fan, *J. Am. Chem. Soc.* **2020**, *142*, 6505−6510.
(53) Z. Wang, O. Chen, C. Y. Cao, K. Finkelstein, D. M. Smilgies, X. Lu, W. A. Bassett, *Rev. Sci. Instrum.* **2010**, *81*, 093902.
(54) Z. Wang, C. Schliehe, T. Wang, Y. Nagaoka, Y. C. Cao, W. A. Bassett, H. Wu, H. Fan, H. Weller, *J. Am. Chem. Soc.* **2011**, *133*, 14484−14487.
(55) T. Wang, R. Li, Z. Quan, W. S. Loc, W. A. Bassett, H. Xu, Y. C. Cao, J. Fang, Z. Wang, *Adv. Mater.* **2015**, *27*, 4544−4549.
(56) J. Zhu, Z. Quan, C. Wang, X. Wen, Y. Jiang, J. Fang, Z. Wang, Y. Zhao, H. Xu, *Nanoscale* **2016**, *8*, 5214−5218.

Supporting Information

Pressure-Stimulus-Responsive Behaviors of Core–Shell InP/ZnSe Nanocrystals: Remarkable Piezochromic Luminescence and Structure Assembly

Hao Liu,[a, b] Yixuan Wang,[a] Xinyi Yang,[a] Xiaohui Zhao,[a] Kai Wang,[a] Min Wu,[a] Xiaobing Zuo,[c] Wenge Yang,[d] Yongming Sui,*[a] and Bo Zou*[a]*

[a] State Key Laboratory of Superhard Materials, College of Physics, Jilin University, Changchun 130012, China

[b] School of Physics and Electronic Engineering, Xinxiang University, Xinxiang 453003, China

[c] X-ray Science Division, Advanced Photon Source, Argonne National Laboratory, Lemont, IL 60439, United States

[d] Center for High Pressure Science and Technology Advanced Research (HPSTAR), Beijing 100094, China

*Corresponding authors: yangxinyi@jlu.edu.cn; suiym@jlu.edu.cn; zoubo@jlu.edu.cn

EXPERIMENTAL DEIAILS

Sample preparation and high-pressure generation.

Synthesis of InP nanocrystals (NCs): InP NCs were synthesized based on the method described in the literature.[1] In a typical synthesis, 0.45 mmol $InCl_3$ and 2.2 mmol $ZnCl_2$ were mixed with 5 mL oleylamine in a 50 mL three-neck flask. The reaction mixture was degassed under vacuum at 120 °C for 30 min and then heated to 190 °C. Next, 0.45 mL (1.6 mmol) tris(diethylamino)phosphine was quickly injected into the reaction flask, and the solution was continuously degassed and purged with nitrogen for 30 min. Afterward, the reaction solution was cooled to room temperature. The InP NCs were precipitated using acetone and centrifuged at 10000 rpm. The precipitate was re-dispersed in toluene and precipitated with acetone. This process was repeated a minimum of three times and the precipitation dried under vacuum for 1 h at 50 °C to get InP NCs powder.

Synthesis of Core−Shell InP/ZnSe NCs: An InP NCs synthesis is performed at 190 °C. Instead of cooling down the temperature, at 20 min: slow injection of 1 mL of saturated TOP-Se (2.2 M). At 60 min: temperature is increased from 190 to 210 °C. At 120 min: slow injection of 1 g of $Zn(stearate)_2$ in 4 mL of octadecene (ODE). Temperature is increased from 210 to 220 °C. At 150 min: injection of 0.7 mL of stoichiometric TOP-Se. Temperature is increased from 220 to 240 °C. At 180 min: slow injection of 0.5 g of $Zn(stearate)_2$ in 2 mL of ODE. Temperature is increased from 240 to 280 °C. At 210 min: injection of 0.7 mL of stoichiometric TOP-Se. Temperature is increased from 280 to 320 °C. At 240 min: slow injection of 0.5 g of $Zn(stearate)_2$ in 2 mL of ODE. At 270 min: end of reaction. At the end of the reaction, the temperature is cooled down. The washing and drying process was the same as that described for InP NCs.

In situ high-pressure measurements: All *in-situ* high-pressure experiments were implemented using Mao-Bell-type[2] symmetric diamond anvil cell (DAC) apparatus furnished with a pair of 400 μm culet diamonds (for pressures up to 40 GPa)[3] at room

temperature. A T301 stainless-steel gasket was pre-indented from a thickness of 250 μm to ~40 μm, and a center hole at 130 μm in diameter was drilled to serve as the sample chamber. The InP/ZnSe powder was loaded into the DAC chamber together with a ruby ball and silicon oil (150 cst, Aldrich). The actual pressure was measured using the standard ruby fluorescence technique.[4] The silicon oil was utilized as the pressure-transmitting medium to provide a hydrostatic environment.[5] Figure S1 shows a schematic demonstration of the sample-loading and stress distribution.

In situ photoluminescence (PL) and absorption micrographs of the samples were obtained using a camera (Canon Eos 5D mark II) equipped on a microscope (Ecilipse TI-U, Nikon). The camera can record the photographs under the same conditions including exposure time and intensity. A semiconductor laser with an excitation wavelength of 355 nm was employed for all PL experiments. Note that all the parameters are fixed completely over each high-pressure PL experiment to avoid the effects of different excitation laser intensities and luminous fluxes on the resulting PL intensity. Meanwhile, the *in-situ* high-pressure absorption spectra were recorded with an optical fiber spectrometer (Ocean Optics, QE65000) using a deuterium-halogen light source.

In situ angle-dispersive X-ray diffraction (ADXRD) patterns of samples under high pressure were recorded at beamline 15U1, Shanghai Synchrotron Radiation Facility (SSRF). Both of the beamline stations at SSRF exploited a monochromatic wavelength of 0.6199 Å. CeO_2 was utilized as the standard sample for the calibration. The Bragg diffraction rings were collected using a Mar-165 CCD detector with an average acquisition time of 30 s for each pressure and then were integrated on the basis of the Dioptas program, yielding 1D intensity versus diffraction angle 2-theta patterns.

In situ small-angle synchrotron X-ray scattering (SAXS) patterns of samples under high pressure were collected at beamline 12-ID-B at the Advanced Photon Source. The monochromatic X-ray radiation of wavelength was λ = 0.4859 Å, and X-ray energy was 13.3 keV. The 2D scattering patterns were radially integrated to

obtain the data of 1D intensity versus q plot, where $q = 4\pi\lambda^{-1} \sin(\theta)$. The d spacing of the lattice constant of the symmetric structure can be calculated by fitting the Bragg peaks in the XRD spectrum, where $d = \lambda/(2\sin\theta) = 2\pi/q$. The lower d spacing (d) is defined as the distance between NCs.

TEM, HRTEM and Size characterization: The resulting samples were characterized by transmission electron microscopy (TEM) and high-resolution TEM performed on a JEM-2200FS with an emission gun operating at 200 kV. The TEM images were introduced into the Nano Measurer 1.2 software and the size of the nanocrystals were calibrated. The calibrated NCs size data were introduced into the originpro2017 software and fitted with Gaussian Function to obtain the average crystallite size of the NCs. The measurement data were finally represented as the mean ± standard error (SE).

The thickness of the formed InP/ZnSe nanosheet was estimated by using the Debye-Scherrer formula[6]:

$$D = 0.89\lambda/(B\cos\theta), \quad (1)$$

where D is the thickness of the InP/ZnSe nanosheet in Å, λ is the wavelength of scattered X-ray in Å, θ is the diffraction angle associated with the first strongest SAXS peak and B is the angular full width at half maximum (FWHM) of the first strongest SAXS peak in rad. The first strongest SAXS peak of post-compression samples was subtracted by baseline and shown in Figure S17. The thickness was estimated by using the FWHM of the first strongest SAXS peak to the Scherrer equation. The thickness of the InP/ZnSe nanosheet is about 27.5 nm, which is equivalent to the thickness of several initial NCs.

Details of PLQY calculation: The PLQY can be calculated using the following formula:[11]

$$\boldsymbol{\Phi = \Phi_R \frac{\int F(\lambda_{em})}{\int F_R(\lambda_{em})} \frac{A_R(\lambda_{ex})}{A(\lambda_{ex})} \frac{n^2}{{n_R}^2}} \quad (2)$$

where Φ is the PLQY, $\int F(\lambda_{em})$ is the integrated intensity of emission, $A(\lambda_{ex})$ is the percentage of light absorbed at excitation wavelength. n is the refractive index, and subscript R denotes the reference data (i.e., the PLQY at ambient pressure). n can be

estimated from the Clausius-Mossotti equation and Lorentz-Lorenz equation:

$$\frac{n^2-1}{n^2+2}\cdot\frac{1}{\rho}=\frac{4\pi}{3}\cdot NA\cdot\alpha=R_{LL} \quad (3)$$

in which the density ρ can be calculated from the cell volume. R_{LL} is called the Lorentz-Lorenz constant. R_{LL} is related to polarizability α. The refractive index n at ambient pressure is 4.489.[12] By this way, the PLQY of InP/ZnSe NCs under high pressures is estimated from the integrated intensity of emission and the percentage of light absorbed at excitation wavelength, as shown in Table S1.

First-principles calculations.

Electronic band structures and structural geometrical optimization for InP were performed using projector augmented waves (PAW) method based on density functional theory as implemented in CASTEP code.[7,8] We used the The Ceperley-Alder localdensity approximation (CA-LDA) was used to describe the exchange-correlation potential.[9] The kinetic cutoff energy was set to 640 eV, and the Brillouin zone was sampled using the Monkhorst-Pack k-points meshes with a resolution of $2\pi \times 0.03$ Å^{-1} to ensure the enthalpy converges to less than 1 meV/atom. Based on the experimental data,[10] the scissor was set 0.7 eV to obtain the final band structure at various pressures.

References

[1] Tessier, M. D.; Dupont, D.; De Nolf, K.; De Roo, J.; Hens, Z. Economic and Size-Tunable Synthesis of InP/ZnE (E = S, Se) Colloidal Quantum Dots. *Chem. Mater.* **2015**, *27*, 4893−4898.

[2] Mao, H.; Bell, P.; Dunn, K.; Chrenko, R.; DeVries, R. Absolute Pressure Measurements and Analysis of Diamonds Subjected to Maximum Static Pressures of 1.3–1.7 Mbar. *Rev. Sci. Instrum.* **1979**, *50*, 1002−1009.

[3] Okamura, H.; Matsunami, M.; Kitamura, R.; Ishida, S.; Ochiai, A.; Nanba, T. Infrared Studies Offelectron Systems under High Pressure Using Synchrotron Radiation. *J. Phys.: Conf. Ser.* **2010**, *215*, 012051.

[4] Mao, H. K.; Xu, J.; Bell, P. M. Calibration of the Ruby Pressure Gauge to 800 kbar under Quasi-Hydrostatic Conditions. *J. Geophys. Res.* **1986**, *91*, 4673−4676.

[5] Klotz, S.; Chervin, J. C.; Munsch, P.; Marchand, G. Hydrostatic Limits of 11 Pressure Transmitting Media. *J. Phys. D: Appl. Phys.* **2009**, *42*, 075413.

[6] Klug, H. P.; Alexander, L. E. *X-ray Diffraction Procedures: For Polycrystalline and Amorphous Materials*, 2nd ed.; Wiley-VCH: New York, **1974**; 992 pp, ISBN 0-471-49369-4.

[7] Kresse, G. From Ultrasoft Pseudopotentials to the Projector Augmented-Wave Method. *Phys. Rev. B* **1999**, *59*, 1758−1775.

[8] Segall, M. D.; Philip, J. D. L.; Probert, M. J.; Pickard, C. J.; Hasnip, P. J.; Clark, S. J.; Payne, M. C. Firstprinciples Simulation: Ideas, Illustrations and the CASTEP Code. *J. Phys.: Condens. Matter* **2002**, *14*, 2717−2744.

[9] Ceperley, D. M.; Alder, B. J. Ground State of the Electron Gas by a Stochastic Method. *Phys. Rev. Lett.* **1980**, *45*, 566−569.

[10] Smith, A. M.; Mohs, A. M.; Nie, S. Tuning the Optical and Electronic Properties of Colloidal Nanocrystals by Lattice Strain[J]. *Nature Nanotechnol.*, **2009**, *4*, 56−63.

[11] Wang, Y.; Guo, S.; Luo, H.; Zhou, C.; Lin, H.; Ma, X.; Hu, Q.; Du, M.-h.; Ma, B.; Yang, W.; Lü, X., Reaching 90% Photoluminescence Quantum Yield in One-Dimensional Metal Halide $C_4N_2H_{14}PbBr_4$ by Pressure-Suppressed Nonradiative Loss. *J. Am. Chem. Soc.* **2020**, *142*, 16001–16006.

[12] Pettit, G. D.; Turner, W. J., Refractive Index of InP. *J. Appl. Phys.* **1965**, *36*, 2081–2081.

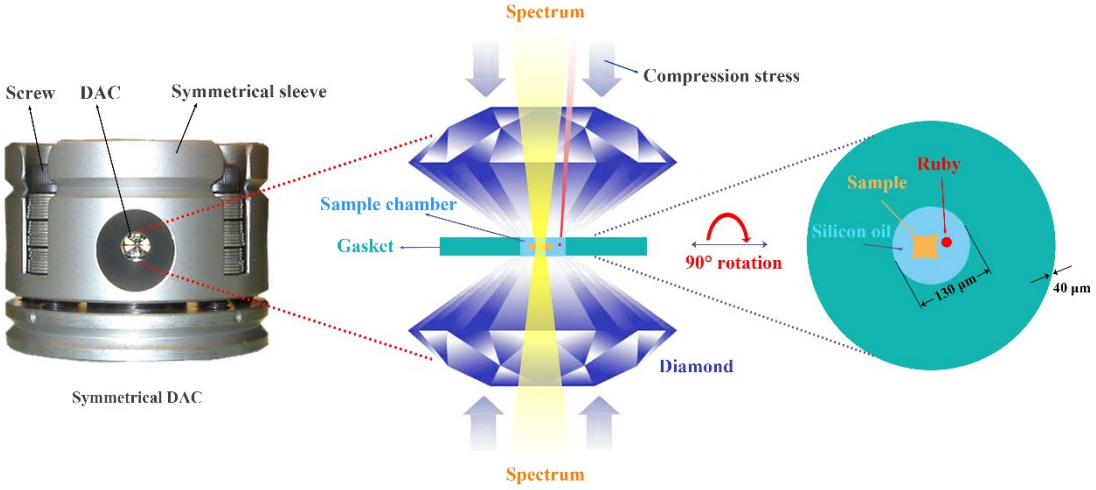

Figure S1 A schematic and detailed presentation of the DAC device. The gasket hole with 130 μm in diameter and 40 μm in thickness was drilled to serve as a sample chamber. The sample was loaded into the chamber together with a ruby ball and silicon oil.

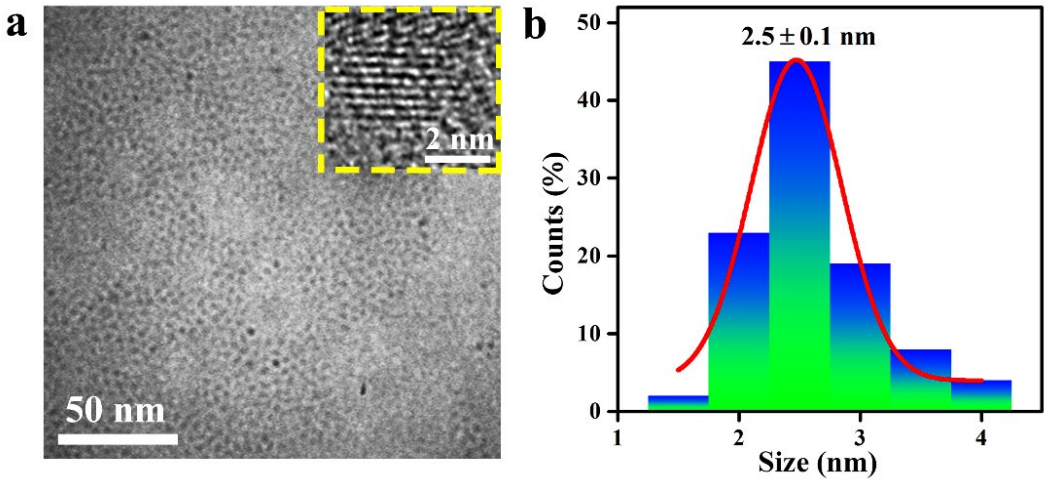

Figure S2 (a) Representative TEM image of the InP NCs. Inset: corresponding HRTEM image. (b) Corresponding size distribution histogram with Gaussian fitting. For size distribution, at least 300 NCs were analyzed, from 3 areas on the sample TEM grid.

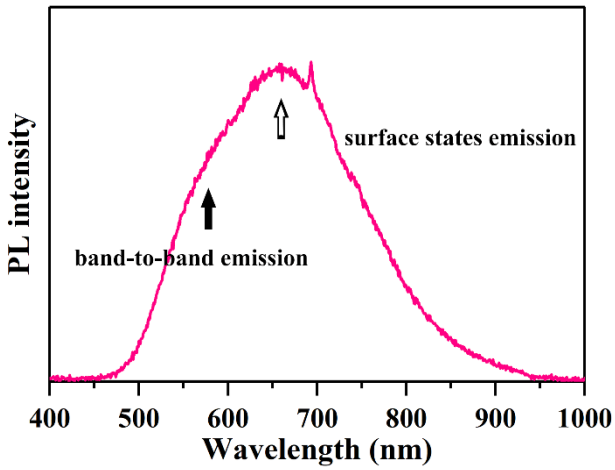

Figure S3 Ambient PL spectrum of the InP NCs. The InP NCs show weak and broad emission in the 500−900 nm region including both band-to-band and surface defect states emissions.

Figure S4 Image of the initial InP/ZnSe powder. The sample was dark brown in color under daylight.

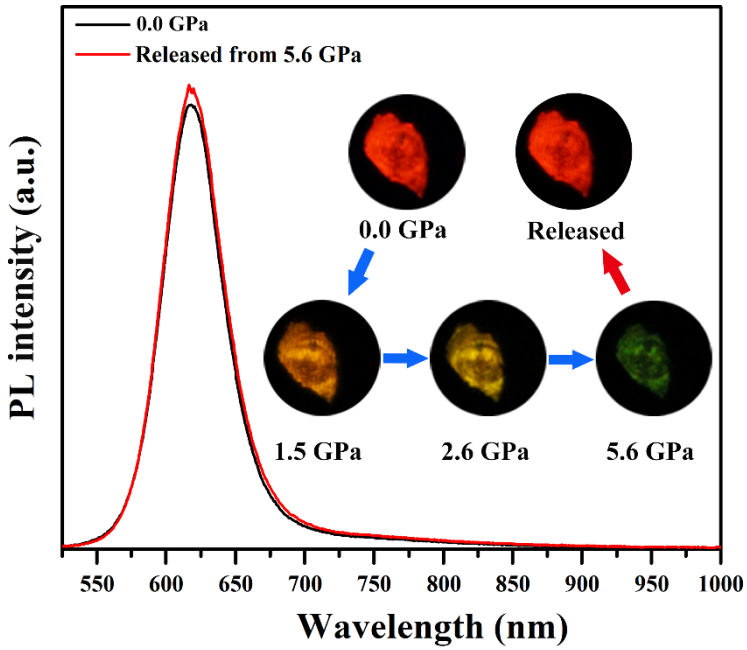

Figure S5 PL peak position and intensity comparison of the InP/ZnSe NCs before and after ~5.6 GPa pressurization. Inset: PL microscopic images of the InP/ZnSe NCs under UV irradiation (λ_{ex} = 355 nm) showing PL color and intensity change under high pressures. After a full pressure cycle of 0−5.6 GPa, the PL peak position and intensity returned to the initial state. This abnormal phenomenon could be reproduced in our repeated experiments.

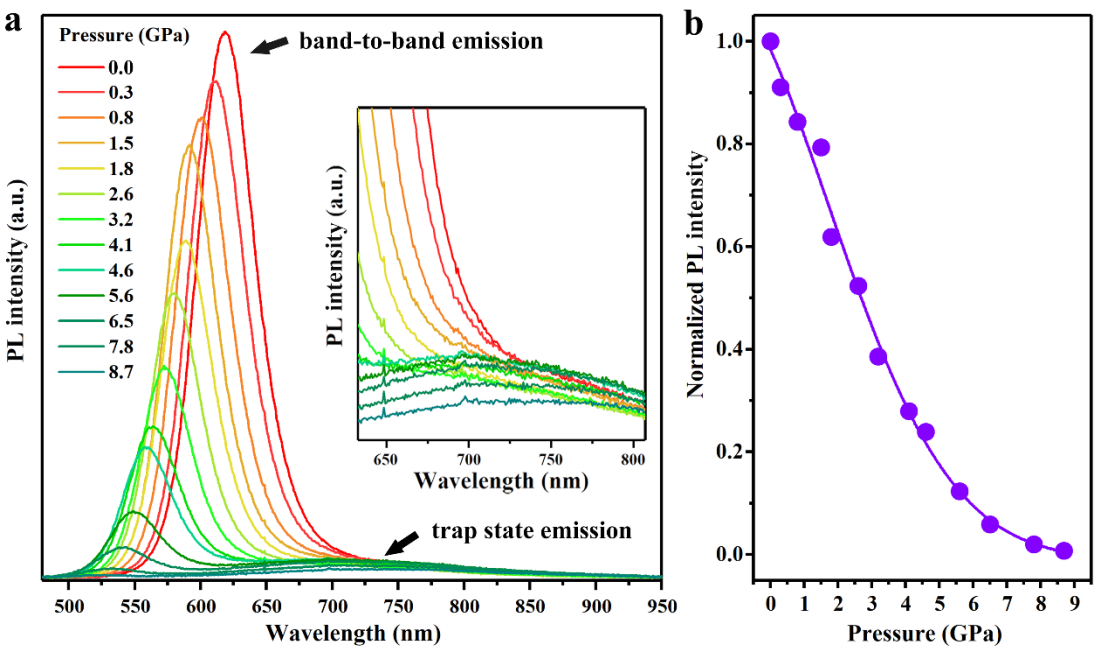

Figure S6 (a) Changes in the PL spectra of the InP/ZnSe NCs with the increase in the pressure from 0 to 8.7 GPa. With the increase in pressure, the intensity of the band-to-band emission spectrum weakened and the peak position blue-shifted until the PL completely disappeared at 8.7 GPa. The trap emission is generally less sensitive to pressure. Inset: The low-energy part of the spectra is zoomed in inset. (b) Normalized PL intensity of the InP/ZnSe NCs as a function of the pressure.

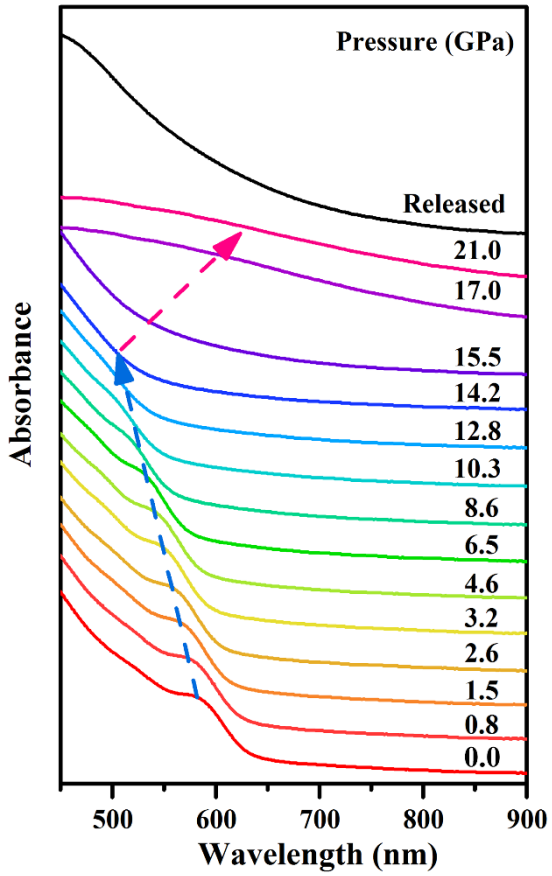

Figure S7 Absorption spectrum of the InP/ZnSe NCs as a function of the pressure. The pressure-dependent absorption spectrum of the InP/ZnSe NCs exhibited a blue-shift with the increase in the pressure from 0 to 14.2 GPa. When a considerably higher pressure (above 14.2 GPa) was applied, an abrupt red-shift was observed up to the maximum pressure study point of 21.0 GPa. When the pressure was released from 21.0 GPa, the absorption edge exhibited a red-shift in comparison with the initial that.

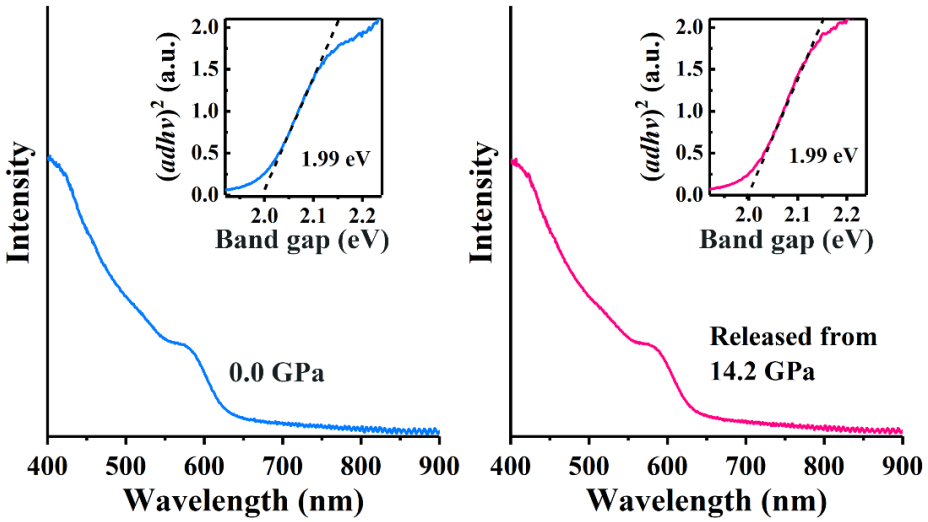

Figure S8 The absorption spectrum and band gap energy comparison of the InP/ZnSe NCs before and after ~14.2 GPa pressurization. Inset: Direct band gap Tauc plot of the InP/ZnSe NCs collected at 0 GPa and 14.2 GPa, respectively. After a compression cycle of 0−14.2 GPa, the absorption spectrum and band gap energy returned to its initial state.

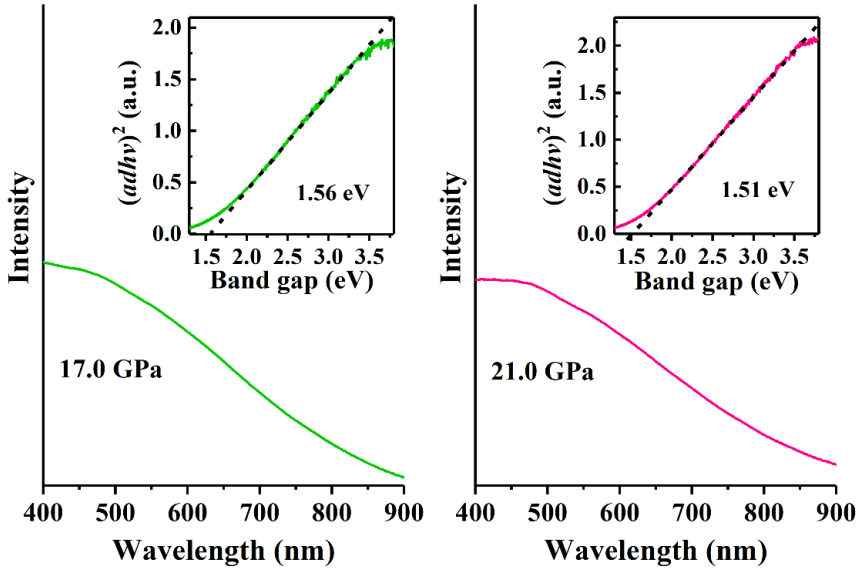

Figure S9 The absorption spectrum and band gap energy of the InP/ZnSe NCs at 17.0 GPa (left) and 21.0 GPa (right), respectively. Inset: corresponding direct band gap Tauc plot of the InP/ZnSe NCs.

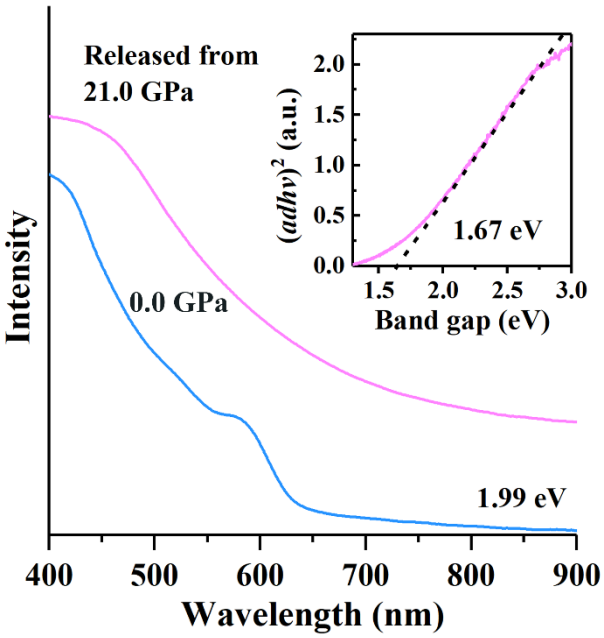

Figure S10 The absorption spectrum and band gap energy comparison of the InP/ZnSe NCs before and after ~21.0 GPa pressurization. Inset: Direct band gap Tauc plot of the InP/ZnSe NCs collected at 21.0 GPa. After a compression cycle of 0−21.0 GPa, the absorption spectrum and band gap energy show a red-shift compared to the initial that.

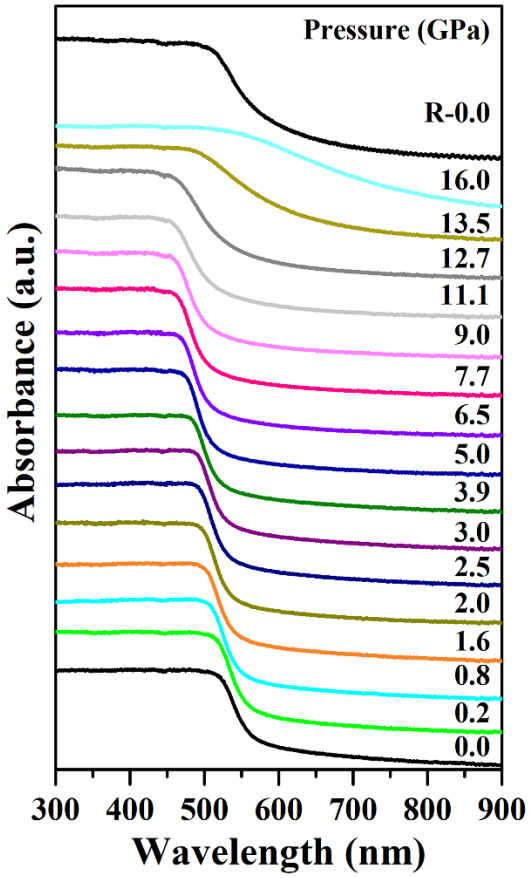

Figure S11 Absorption spectrum of the InP NCs as a function of the pressure.

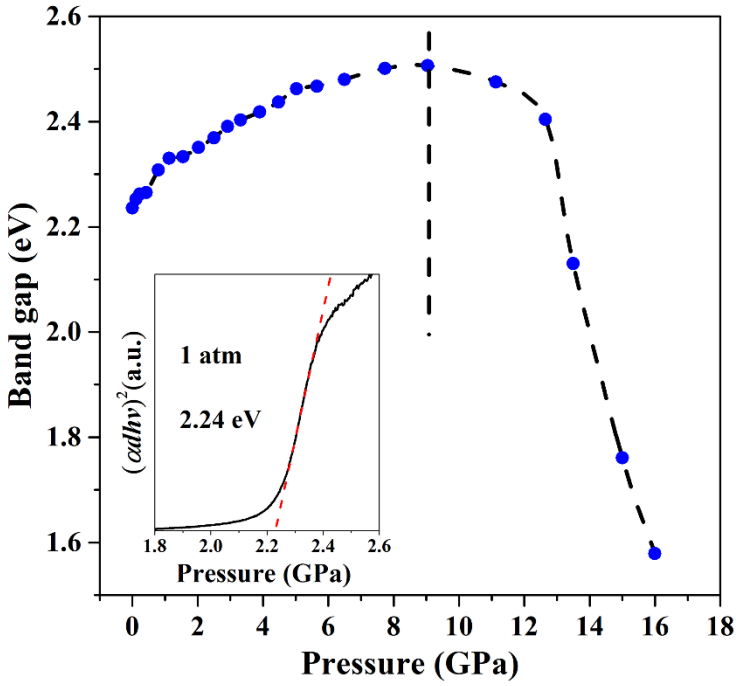

Figure S12 Shift of the bandgap energy of the InP NCs with pressure. Inset shows the Tauc plot of the InP NCs under ambient conditions.

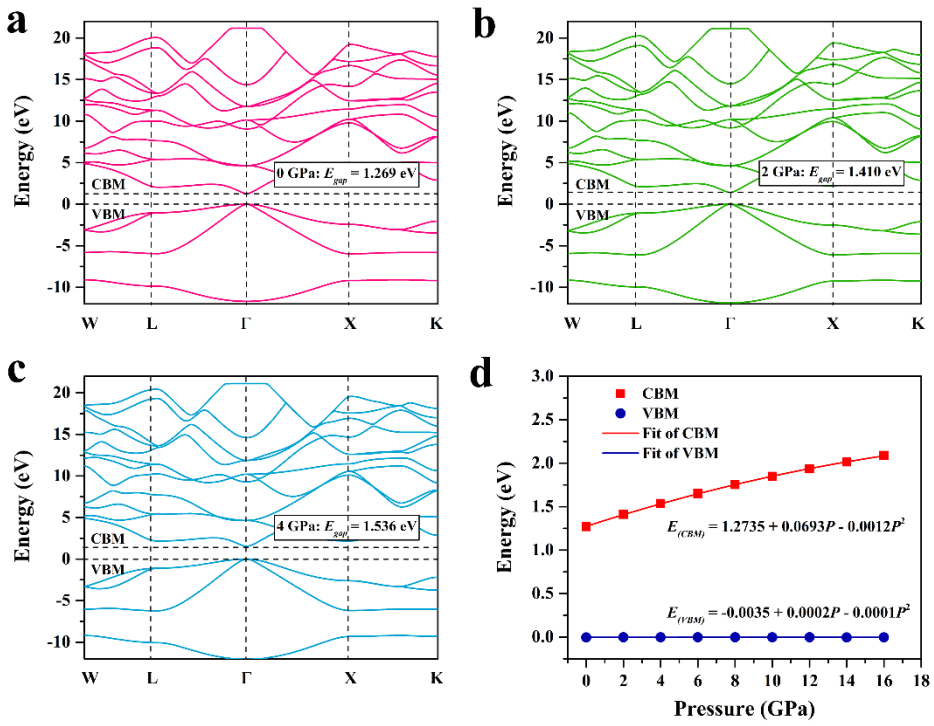

Figure S13 Energy band of InP at different pressures, (a) 0 GPa; (b) 2 GPa; (c) 4 GPa. (d) Energy of conduction band minimum (CBM) and valence band maximum (VBM) of InP with increasing pressure.

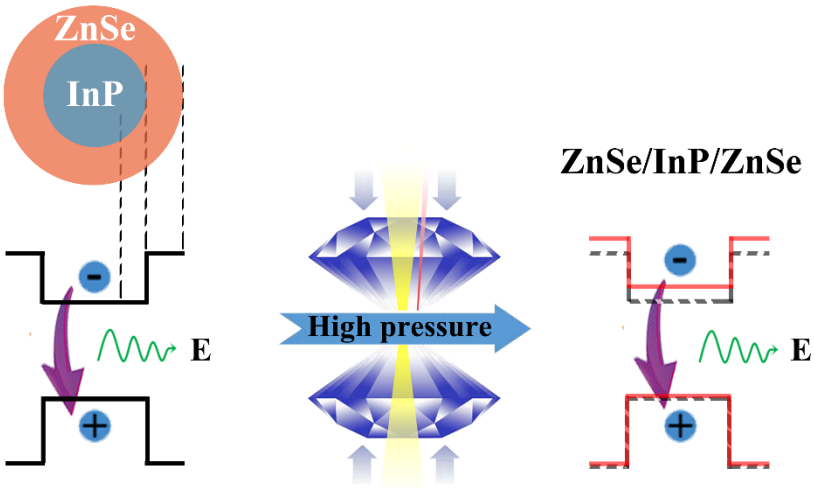

Figure S14 Schematic illustration of electronic energy levels for InP/ZnSe core/shell NCs at ambient conditions (left) and high pressure (right). The red lines depict the the changed energy levels under pressure, and dashed lines are the intrinsic band alignments.

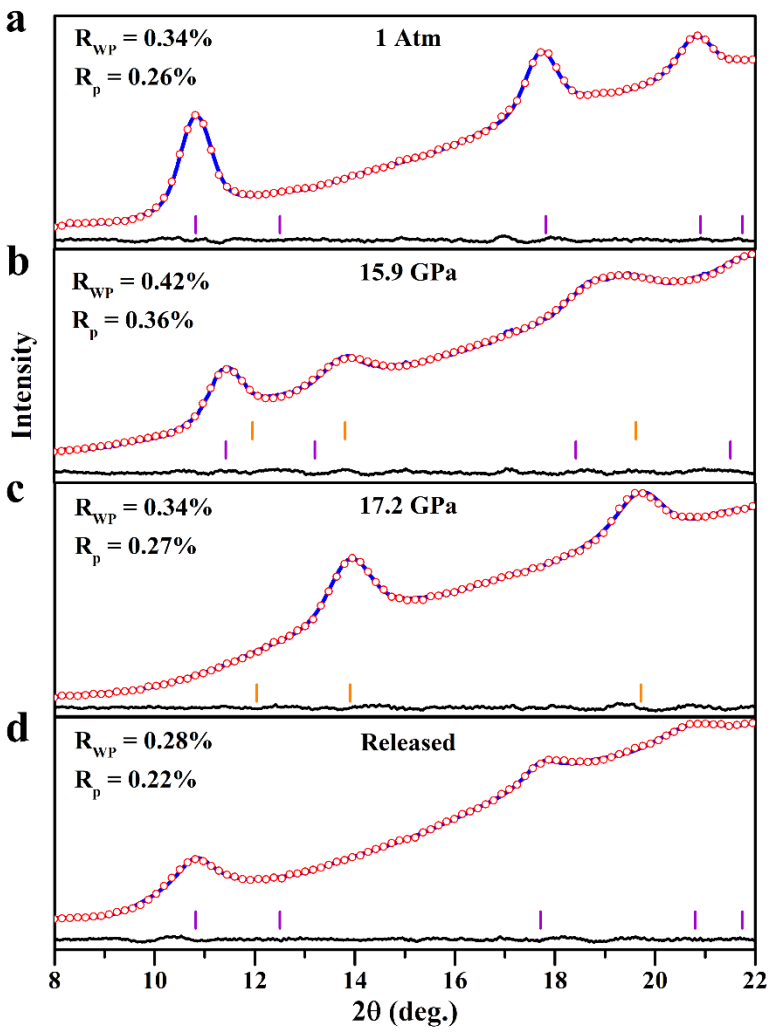

Figure S15 Rietveld refinements of the experimental (blue line), simulated (red circles), and difference (black line) ADXRD patterns of ZB structure at 0 GPa (a), mixed-structures at 15.9 GPa (b), RS structure at the pressure of 17.2 GPa (c), and ZB structure acquired after releasing the pressure from 21.5 GPa (d). Purple and orange vertical markers indicate the corresponding Bragg reflections of ZB and RS structure, respectively.

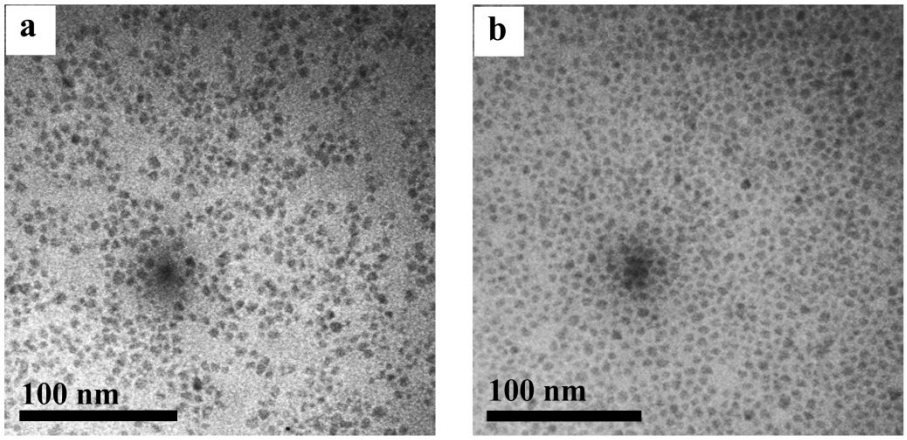

Figure S16 (a) Representative TEM image of the InP/ZnSe NCs, acquired after releasing the pressure from about 9.0 GPa. (b) Representative TEM image of the InP/ZnSe NCs, acquired after releasing the pressure from about 14.0 GPa.

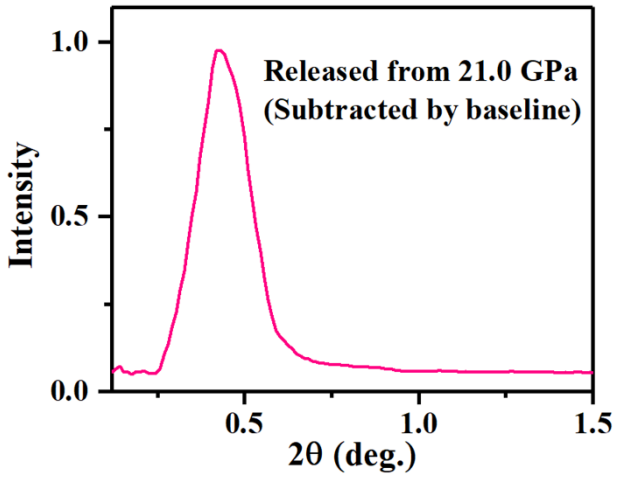

Figure S17 The SAXS spectrum (first SAXS peak) of post-compression samples was subtracted by baseline.

Table S1 The PLQYs of InP/ZnSe NCs under different pressure.

Pressure (GPa)	PL integral intensity I/I_0	Cell volume V/V_0	Refractive index square n^2	PLQY
0.0	1.000	1.000	20.151	30.09
0.6	0.836	0.992	21.408	26.72
1.7	0.616	0.979	23.727	21.83
2.5	0.524	0.970	25.793	20.18
3.5	0.417	0.958	28.778	17.92
6.6	0.192	0.924	45.118	12.94
7.7	0.139	0.911	57.604	11.96